2026 IEEE International Conference on Robotics and Automation (ICRA 2026)
June 1-5, 2026. Vienna, Austria

Backdrivable Redundantly Actuated Parallel Robot for Sensorless Physical Human-Robot Interaction

Arda Yiğit[1], Simon Foucault[2] and Clément Gosselin[2]

***Abstract*— This paper introduces a new redundantly actuated parallel robot capable of sensorless physical human-robot interaction. Three 3-DoF legs are attached to an end-effector platform through spherical joints. This architecture alleviates most parallel singularities, thus enabling a very large workspace. The use of quasi-direct-drive actuators yields a backdrivable robot with very low impedance, since all actuators are fixed to the base. Furthermore, since the actuators are force/torque controlled, internal antagonistic forces can be controlled without additional sensing devices. Experiments are carried out on a physical prototype and validate the large workspace and physical interaction capabilities of the robot.**

I. Introduction

Physical human-robot interaction (pHRI) requires developing robotic systems to assist operators during the execution of given tasks without compromising operator safety. Most industrial robots with pHRI capabilities are serial robot arms. While these robots provide a large workspace, one can question their relevance for intuitive pHRI. Indeed, to reduce the moving mass, serial robot arms are actuated by geared motors. The use of gearboxes significantly increases the inertia reflected at the end-effector since the inertia of the rotating part of the actuators is amplified by the square of the reduction ratio. Furthermore, with a high reduction ratio, actuators lose backdrivability due to friction; therefore, force/torque (F/T) sensors are required. The combination of these characteristics yields high-impedance interactive devices, especially at high frequency.

Using parallel robot architectures to design collaborative robots can overcome these drawbacks. Since the actuators of a parallel robot can be fixed at the base, geared motors can be replaced with direct-drive actuators, thereby significantly reducing the reflected inertia at the end-effector and providing mechanical backdrivability. Some haptic devices adopt this solution [1], [2], [3]. However, parallel robots have their own limitations, such as singularities within their workspace, mechanical interference between legs, or nonlinear stiffness characteristics. Kinematically redundant designs can solve some of these issues by introducing additional actuated joints in one or more legs of a parallel mechanism [4]. Singularities within the workspace restrict the orientation capabilities of parallel robots. Typically, the maximum tilt angle of the well-known Stewart platform is approximately $45°$. The orientational workspace of a Stewart-like platform can be extended by replacing some of the legs with redundant legs comprising two sub-legs, each containing a prismatic joint [5], [6]. The two sub-legs are connected to a spherical joint on the platform through a revolute joint and an additional link. With proper design, it is even possible to obtain a singularity-free robot [7]. Then, the redundancy can be used for other tasks, such as the remote actuation of an articulated platform or sensing the operator intention [8], [9].

Actuation redundancy is yet another promising approach to overcome the limitations of parallel robots [10], [11]. A parallel robot is said to be redundantly actuated if it uses more actuators than its degree of mobility. Redundant actuation can be implemented by adding extra legs to the mechanism [12] or by actuating the passive joints of an existing architecture [13]. Redundantly actuated parallel robots are less prone to singularities since there are infinitely many solutions for actuated joint torques to generate a desired wrench at the end-effector [14]. Such robots also benefit from higher stiffness [15] and better accuracy [16]. Yet, potential internal antagonistic forces must be dealt with using load cells or force/torque sensors [17] and appropriate control algorithms [18].

In this work, we propose a new class of backdrivable redundantly actuated parallel robots for sensorless pHRI. Three three-degree-of-freedom legs are connected to an end-effector platform through spherical joints, with each leg consisting of a parallel mechanism. The redundantly actuated architecture alleviates most parallel singularities, yielding a very large workspace, especially for orientations. The robot is actuated by direct-drive motors using a backdrivable transmission with a very low reduction ratio. Therefore, the end-effector wrench and the internal forces can be controlled without requiring any force/torque sensors or load cells. An impedance controller enables safe physical interaction. As an example of the implementation of the novel class of robots, experiments are carried out using a novel three-legged robot based on the RU/2-RUS leg mechanism presented in [19], [20]. These experiments validate the large workspace of the robot and the high-bandwidth interaction capabilities. To the best of our knowledge, the proposed robot is the first redundantly actuated parallel robot enabling seamless physical human-robot interaction without requiring any force/torque sensors. Therefore, it benefits from actuation redundancy to enlarge the workspace without suffering from the drawbacks of force/torque sensors (such as communication delays,

*This work was supported by the Natural Sciences and Engineering Research Council of Canada (NSERC). This article has supplementary downloadable material (video) provided by he authors.

[1]Arda Yiğit is with the Laboratoire des Sciences du Numérique de Nantes, Centre National de la Recherche Scientifique, 44321 Nantes, France (e-mail: arda.yigit@ls2n.fr).

[2]Simon Foucault and Clément Gosselin are with the Department of Mechanical Engineering, Université Laval, Québec, QC G1V 0A6, Canada (e-mail: foucault@gmc.ulaval.ca; gosselin@gmc.ulaval.ca).

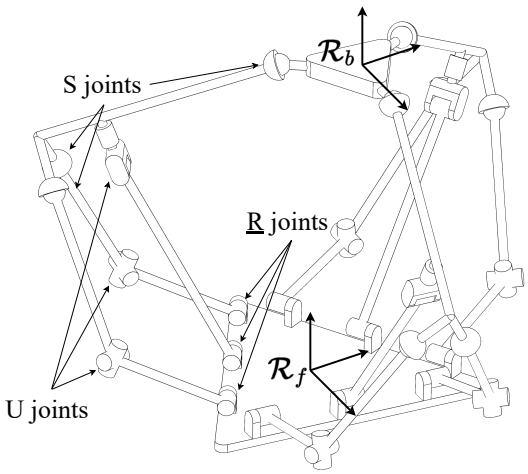

Fig. 1: Architecture of the redundantly actuated parallel robot.

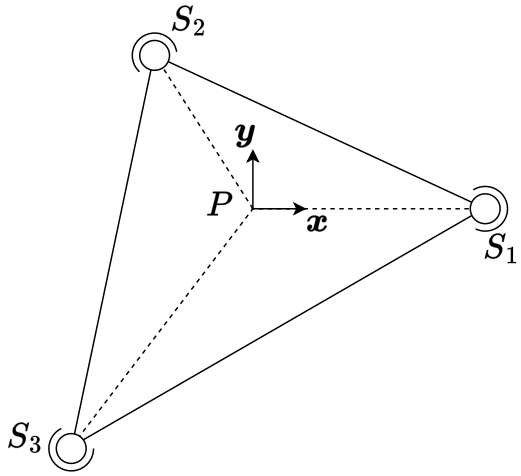

Fig. 2: Parametrization of the platform.

structural compliance, and filtering that limit closed-loop dynamics).

The structure of the paper is as follows. The kinematic and dynamic models of the considered class of robots are presented in Section II. An impedance control law is introduced in Section III. The experimental setup is described in Section IV. Finally, the experimental results are reported in Section V, and conclusions and perspectives are presented in Section VI.

II. Modelling

The considered robot has three three-degree-of-freedom legs connected to an end-effector platform through spherical joints. An example of such a robot is illustrated in Fig. 1. This robot uses the parallel leg mechanism introduced by the authors in [19], but other mechanisms can be considered as well (see, for instance, [21], [22]). Globally, the robot has six degrees of freedom and nine actuators (three in each leg), therefore the redundant actuation.

The parametrization of the platform is shown in Fig. 2. Vectors $\boldsymbol{x}$ and $\boldsymbol{y}$ lie within the plane of the platform. Without loss of generality, vector $\boldsymbol{x}$ is considered to point from the reference point P on the platform towards the centre of the first spherical joint S_1. Vector $\boldsymbol{z}$ is orthogonal to the plane of the platform and is obtained using the right-hand rule.

In the remaining of the paper, the following notations are used. The position vector of a point A is noted $\boldsymbol{a}$. The orientation of the body frame $\mathcal{R}_b = (P, \boldsymbol{x}, \boldsymbol{y}, \boldsymbol{z})$ attached to the platform with respect to an inertial frame $\mathcal{R}_f$ attached to the base is $\boldsymbol{R}$. The end-effector twist is $\boldsymbol{t} = [\dot{\boldsymbol{p}}^T \ \boldsymbol{\omega}^T]^T$, with $\boldsymbol{\omega}$ the angular velocity. The ith spherical joint is located at S_i.

A. Kinematics

This subsection only deals with platform kinematics since the leg kinematics depends on the selected leg mechanism.

The inverse kinematic problem aims at finding the input coordinates, i.e., the positions $\boldsymbol{s}_i$ of the spherical joints, from the output coordinates, i.e., the pose $(\boldsymbol{p}, \boldsymbol{R})$ of the end-effector. Since vectors $\boldsymbol{u} = \boldsymbol{s}_i - \boldsymbol{p}$ are constant in the body frame $\mathcal{R}_b$, the solution of the inverse kinematics is

$$\boldsymbol{s}_i = \boldsymbol{p} + \boldsymbol{R}^b \boldsymbol{u}. \tag{1}$$

The forward kinematic problem consists in determining the output coordinates, i.e., the pose $(\boldsymbol{p}, \boldsymbol{R})$ of the end-effector, from the input coordinates, i.e., the position of each of the spherical joints.

Knowing the position of each of the spherical joints, S_i, the position vector $\boldsymbol{p}$ can be readily obtained since it is a constant linear combination of $\boldsymbol{s}_2 - \boldsymbol{s}_1$ and $\boldsymbol{s}_3 - \boldsymbol{s}_1$, where the constant coefficients are obtained from the geometry of the platform. The rotation matrix $\boldsymbol{R}$ can be written as $\boldsymbol{R} = [\boldsymbol{x}\ \boldsymbol{y}\ \boldsymbol{z}]$. The unit vector $\boldsymbol{z}$ is orthogonal to the plane of the platform, therefore,

$$\boldsymbol{z} = \frac{(\boldsymbol{s}_2 - \boldsymbol{s}_1) \times (\boldsymbol{s}_3 - \boldsymbol{s}_1)}{\|(\boldsymbol{s}_2 - \boldsymbol{s}_1) \times (\boldsymbol{s}_3 - \boldsymbol{s}_1)\|}. \tag{2}$$

Then, the unit vector $\boldsymbol{x}$ is obtained by rotating $\boldsymbol{s}_1 - \boldsymbol{s}_2$ about $\boldsymbol{z}$ by an angle θ, using Rodrigues' formula

$$\boldsymbol{x} = (\boldsymbol{s}_1 - \boldsymbol{s}_2)c_\theta + [\boldsymbol{z} \times (\boldsymbol{s}_1 - \boldsymbol{s}_2)]s_\theta + \boldsymbol{z}[\boldsymbol{z}^T(\boldsymbol{s}_1 - \boldsymbol{s}_2)](1 - c_\theta) \tag{3}$$

with $c_\theta = \cos\theta$ and $s_\theta = \sin\theta$ and where θ is a constant angle obtained a priori from the geometry of the platform. Finally, we have $\boldsymbol{y} = \boldsymbol{z} \times \boldsymbol{x}$.

B. Jacobian Matrices

The relationship between the position of the spherical joints and the end-effector twist is

$$\dot{\boldsymbol{s}}_i = \dot{\boldsymbol{p}} + (\boldsymbol{p} - \boldsymbol{s}_i) \times \boldsymbol{\omega}, \tag{4}$$

which yields the Jacobian matrix

$$\dot{\boldsymbol{s}} = \underbrace{\begin{bmatrix} \boldsymbol{I}_3 & [\boldsymbol{p} - \boldsymbol{s}_1]_\times \\ \boldsymbol{I}_3 & [\boldsymbol{p} - \boldsymbol{s}_2]_\times \\ \boldsymbol{I}_3 & [\boldsymbol{p} - \boldsymbol{s}_3]_\times \end{bmatrix}}_{\boldsymbol{J}_p} \boldsymbol{t} \tag{5}$$

where $\boldsymbol{s} = [\boldsymbol{s}_1^T \ \boldsymbol{s}_2^T \ \boldsymbol{s}_3^T]^T$ and $[\cdot]_\times$ is the cross product matrix. It can be noted that the Jacobian matrix $\boldsymbol{J}_p$ is constant if vectors are expressed in the body frame $\mathcal{R}_b$. Furthermore, $\operatorname{rank} \boldsymbol{J}_p = 6$ as long as points S_i are not aligned. Also, it is observed that the Jacobian matrix is not square due to actuation redundancy.

The leg kinematics describe the relationship between the movements of the actuated joints and those of points S_i, namely

$$\boldsymbol{J}_{li}\dot{\boldsymbol{s}}_i = \boldsymbol{K}_{li}\dot{\boldsymbol{q}}_i, \qquad i = 1, 2, 3 \tag{6}$$

with $\boldsymbol{J}_{li}$ and $\boldsymbol{K}_{li}$ Jacobian matrices and $\boldsymbol{q}_i$ the coordinates of the actuated joints of the ith leg. The expressions of the Jacobian matrices associated with the leg mechanism considered in this paper were derived in a previous work [19]. Let $\boldsymbol{J}_l$ and $\boldsymbol{K}_l$ be block diagonal matrices whose diagonal entries are respectively $\boldsymbol{J}_{li}$ and $\boldsymbol{K}_{li}$. Hence,

$$\boldsymbol{J}_l\dot{\boldsymbol{s}} = \boldsymbol{K}_l\dot{\boldsymbol{q}} \tag{7}$$

with $\boldsymbol{q} = [\boldsymbol{q}_1^T \ \boldsymbol{q}_2^T \ \boldsymbol{q}_3^T]^T$.

Finally, combining (5) and (7) yields the global kinematics

$$\boldsymbol{J}_l\boldsymbol{J}_p\boldsymbol{t} = \boldsymbol{K}_l\dot{\boldsymbol{q}}. \tag{8}$$

C. Singularities

Serial singularities (or type I) occur when a nonzero input velocity $\dot{\boldsymbol{q}}$ produces a zero twist $\boldsymbol{t}$ [23]. This happens only if $\det \boldsymbol{K}_l = 0$. Therefore, the serial singularities of the parallel robot are those of the leg mechanisms.

Parallel (or type II) singularities correspond to situations in which the end-effector can locally move even when the actuators are locked [23]. Equivalently, a parallel singularity occurs when $\operatorname{rank}(\boldsymbol{J}_l\boldsymbol{J}_p) < 6$. For a kinematically redundant parallel robot similar to the robot introduced here but with an articulated platform, it was shown that the platform can be designed such that the robot is in a parallel singularity if and only if at least one leg is in a parallel singularity [8]. With actuation redundancy, under some conditions, it is possible to avoid the parallel singularity of the robot while some of the legs are in singular configurations. An example is now given to illustrate this behaviour.

Assume that legs 1 and 2 are not in a singular configuration. Let us define

$$\boldsymbol{J}_{12} = \begin{bmatrix} \boldsymbol{J}_{l1} & \boldsymbol{0} \\ \boldsymbol{0} & \boldsymbol{J}_{l2} \end{bmatrix} \underbrace{\begin{bmatrix} \boldsymbol{I}_3 & [\boldsymbol{p} - \boldsymbol{s}_1]_\times \\ \boldsymbol{I}_3 & [\boldsymbol{p} - \boldsymbol{s}_2]_\times \end{bmatrix}}_{\boldsymbol{J}_{p12}}. \tag{9}$$

Then, $\operatorname{rank} \boldsymbol{J}_{12} = \operatorname{rank} \boldsymbol{J}_{p12} = 5$ and $\boldsymbol{n} = [\boldsymbol{u}^T \ \boldsymbol{v}^T]^T$ spans $\ker \boldsymbol{J}_{12} = \ker \boldsymbol{J}_{p12}$ with $\boldsymbol{u} = (\boldsymbol{p} - \boldsymbol{s}_1) \times (\boldsymbol{s}_1 - \boldsymbol{s}_2)$ and $\boldsymbol{v} = \boldsymbol{s}_2 - \boldsymbol{s}_1$.

Therefore, $\boldsymbol{n} \in \ker(\boldsymbol{J}_l\boldsymbol{J}_p)$ if and only if

$$\boldsymbol{J}_{l3}\left[(\boldsymbol{s}_3 - \boldsymbol{s}_1) \times (\boldsymbol{s}_2 - \boldsymbol{s}_1)\right] = \boldsymbol{0} \tag{10}$$

As a consequence, the robot is in a singular configuration if and only if $\boldsymbol{z} \in \ker \boldsymbol{J}_{l3}$ or points S_1, S_2 and S_3 are aligned. Hence, the third leg does not need to be in a non-singular configuration. It suffices that the nullspace of the Jacobian matrix of the third leg does not include vector $\boldsymbol{z}$. This property is of great interest because it means that the type II singularities of the legs may be alleviated by properly distributing the forces in the legs.

D. Dynamics

If the mass of the platform is noted m_p and its inertia matrix with respect to its centre of mass is noted $\boldsymbol{I}_p$, we have

$$\underbrace{\begin{bmatrix} m_p\boldsymbol{I}_3 & \boldsymbol{0} \\ \boldsymbol{0} & \boldsymbol{I}_p \end{bmatrix}}_{\boldsymbol{M}_p} \dot{\boldsymbol{t}} + \underbrace{\begin{bmatrix} \boldsymbol{0} & \boldsymbol{0} \\ \boldsymbol{0} & [\boldsymbol{\omega}]_\times \boldsymbol{I}_p \end{bmatrix}}_{\boldsymbol{C}_p} \boldsymbol{t} + \underbrace{\begin{bmatrix} m_p\boldsymbol{g}_r \\ \boldsymbol{0} \end{bmatrix}}_{\boldsymbol{g}_p} = \boldsymbol{J}_p^T\boldsymbol{f} - \boldsymbol{w}_e \tag{11}$$

with $\boldsymbol{f} = [\boldsymbol{f}_1^T \ \boldsymbol{f}_2^T \ \boldsymbol{f}_3^T]^T$ the forces applied by the leg mechanisms to the platform at the spherical joints, $\boldsymbol{w}_e$ an external wrench and $\boldsymbol{g}_r$ the gravitational acceleration vector. In the above, it is assumed that the reference point P on the platform coincides with the centre of mass of the platform.

Let us consider that the robot is actuated by identical motors with inertia I_m and that the mass and inertia of the links are neglected. Then, we have

$$I_m\ddot{\boldsymbol{q}}_{li} = \boldsymbol{\tau}_i - (\boldsymbol{K}_{li}^{-1}\boldsymbol{J}_{li})^{-T}\boldsymbol{f}_i \tag{12}$$

with $\boldsymbol{\tau}_i = [\tau_{i1} \ \tau_{i2} \ \tau_{i3}]^T$ the array containing the torques generated by the actuators of the ith leg and $\boldsymbol{q}_{li}$ the array containing the coordinates of the actuators of the ith leg. Hence, we have

$$\boldsymbol{f} = (\boldsymbol{K}_l^{-1}\boldsymbol{J}_l)^T(\boldsymbol{\tau} - I_m\ddot{\boldsymbol{q}}) \tag{13}$$

with $\boldsymbol{q} = [\boldsymbol{q}_{l1}^T \ \boldsymbol{q}_{l2}^T \ \boldsymbol{q}_{l3}^T]^T$ and $\boldsymbol{\tau} = [\boldsymbol{\tau}_1^T \ \boldsymbol{\tau}_2^T \ \boldsymbol{\tau}_3^T]^T$.

Taking the time derivative of the global kinematics (8) yields

$$\ddot{\boldsymbol{q}} = \boldsymbol{J}\dot{\boldsymbol{t}} + \dot{\boldsymbol{J}}\boldsymbol{t} \tag{14}$$

with $\boldsymbol{J} = \boldsymbol{K}_l^{-1}\boldsymbol{J}_l\boldsymbol{J}_p$. The derivative of $\boldsymbol{J}$ can be expressed analytically using the formula $\frac{d}{dt}(\boldsymbol{A}^{-1}) = -\boldsymbol{A}^{-1}\frac{d}{dt}(\boldsymbol{A})\boldsymbol{A}^{-1}$.

Combining (11), (13) and (14) yields

$$\boldsymbol{M}\dot{\boldsymbol{t}} + \boldsymbol{C}\boldsymbol{t} + \boldsymbol{g} = \boldsymbol{J}^T\boldsymbol{\tau} - \boldsymbol{w}_e \tag{15}$$

with

$$\begin{cases} \boldsymbol{M} & = \boldsymbol{M}_p + I_m\boldsymbol{J}^T\boldsymbol{J} \\ \boldsymbol{C} & = \boldsymbol{C}_p + I_m\boldsymbol{J}^T\dot{\boldsymbol{J}} \\ \boldsymbol{g} & = \boldsymbol{g}_p \end{cases}. \tag{16}$$

III. Control

We define the current pose of the end-effector $\boldsymbol{g} = (\boldsymbol{p}, \boldsymbol{R}) \in SE(3)$ and the target pose $\boldsymbol{g}_* = (\boldsymbol{p}_*, \boldsymbol{R}_*) \in SE(3)$. The target twist is $\boldsymbol{t}_* \in se(3)$. The quaternion $(\eta, \boldsymbol{\mu})$ describes the rotation $\boldsymbol{R}^T\boldsymbol{R}_*$ between the current frame and the desired frame.

The impedance controller is of the form

$$\boldsymbol{J}^T\boldsymbol{\tau} = \boldsymbol{M}\dot{\boldsymbol{t}}_* + (\boldsymbol{C} + \boldsymbol{D})(\boldsymbol{t}_* - \boldsymbol{t}) + \tilde{\boldsymbol{K}}\zeta + \boldsymbol{C}\boldsymbol{t} + \boldsymbol{g} \tag{17}$$

with $\zeta = \boldsymbol{g}_* \ominus \boldsymbol{g} = [(\boldsymbol{p}_* - \boldsymbol{p})^T \ \boldsymbol{\mu}^T]^T$ the configuration error and $\boldsymbol{D}$ a positive semidefinite matrix. The impedance control law is illustrated in Fig. 3.

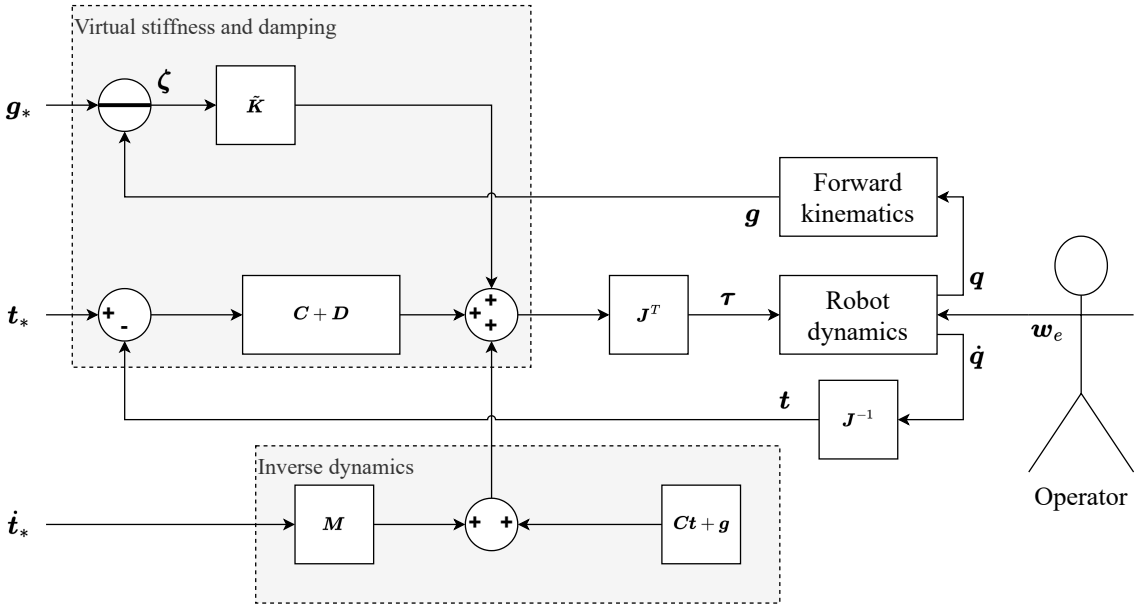

Fig. 3: Control diagram.

The solution $\boldsymbol{\tau}$ to (17) is not unique. The chosen solution is

$$\boldsymbol{\tau} = (\boldsymbol{J}^T)^+\boldsymbol{u} + \boldsymbol{N}_J\boldsymbol{\tau}_0 \tag{18}$$

with $\boldsymbol{u}$ the r.h.s. of (17), $(\boldsymbol{J}^T)^+ = \boldsymbol{W}^{-1}\boldsymbol{J}(\boldsymbol{J}^T\boldsymbol{W}^{-1}\boldsymbol{J})^{-1}$ a generalized inverse of $\boldsymbol{J}^T$, $\boldsymbol{W}$ a positive definite weighting matrix, $\boldsymbol{N}_J = \boldsymbol{I}_9 - (\boldsymbol{J}^T)^+\boldsymbol{J}^T$ a projector within the nullspace of $\boldsymbol{J}^T$ and $\boldsymbol{\tau}_0$ a desired prestress.

In order to assess the passivity of the closed-loop system, let us consider the positive definite storage function written as

$$V = \frac{1}{2}(\boldsymbol{t}_* - \boldsymbol{t})^T\boldsymbol{M}(\boldsymbol{t}_* - \boldsymbol{t}) + \frac{1}{2}\boldsymbol{\zeta}^T\boldsymbol{K}\boldsymbol{\zeta}. \tag{19}$$

The time derivative of this function verifies

$$\dot{V} \leq (\boldsymbol{t}_* - \boldsymbol{t})^T\boldsymbol{w}_e - (\boldsymbol{t}_* - \boldsymbol{t})^T\tilde{\boldsymbol{K}}\boldsymbol{\zeta} + \dot{\boldsymbol{\zeta}}^T\boldsymbol{K}\boldsymbol{\zeta}. \tag{20}$$

Following the suggestion of Caccavale et al. [24], let $\tilde{\boldsymbol{K}}$ be defined as

$$\tilde{\boldsymbol{K}} = \begin{bmatrix} \boldsymbol{I} & \boldsymbol{0} & \boldsymbol{0} \\ \boldsymbol{0} & \frac{1}{2}(\eta\boldsymbol{I} + [\boldsymbol{\mu}]_\times) & \boldsymbol{0} \\ \boldsymbol{0} & \boldsymbol{0} & \boldsymbol{I} \end{bmatrix}\boldsymbol{K} \tag{21}$$

with $\boldsymbol{K}$ a positive semidefinite matrix. Using quaternion propagation yields $(\boldsymbol{t}_* - \boldsymbol{t})^T\tilde{\boldsymbol{K}} = \dot{\boldsymbol{\zeta}}^T\boldsymbol{K}$. Therefore,

$$\dot{V} \leq (\boldsymbol{t}_* - \boldsymbol{t})^T\boldsymbol{w}_e. \tag{22}$$

Hence, the closed-loop system is passive with respect to the pair $(\boldsymbol{w}_e, \boldsymbol{t}_* - \boldsymbol{t})$.

To assess the stability of the closed-loop system, the storage function (19) can be considered as a Lyapunov candidate function. From LaSalle's invariance principle, asymptotic stability is reached if $\boldsymbol{D}$ and $\boldsymbol{K}$ are positive definite.

IV. Experimental Setup

The prototype is shown in Fig. 4. The architecture corresponds to the one illustrated in Fig. 1. The leg mechanism is optimally designed to provide intuitive pHRI by maximizing the workspace in which the end-effector of the leg can have a $2g$ acceleration in all directions.

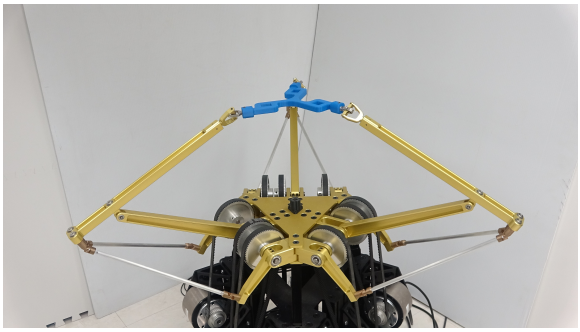

Fig. 4: Prototype.

The links of the robot are made of aluminum, except for the universal joints, which are made of brass for better compactness. The platform is 3D-printed. Large orientation capabilities highly depend on the range of motion of the spherical joints. This prototype uses 4-DoF spherical joints with $\pm 150°$ range of motion introduced by Schreiber and Gosselin [25].

The prototype is actuated by nine identical SGMCS-05B3B-YAX1 direct-drive motors with $5\,\mathrm{Nm}$ nominal torque and nine SGD7S-2R8FA0A drives from Yaskawa. In order to reduce the footprint of the robot, timing belts connect the actuators to the actuated revolute joints. The transmission ratio is $72/34 \approx 2.12$, so the nominal torque available at the actuated joints is close to $10\,\mathrm{Nm}$. The actuators are equipped with 20-bit encoders. Joint velocities are obtained

(a) (b) (c) (d)

Fig. 5: Illustration of the robot workspace: (a) 90° tilt, (b) 75° torsion, (c) large horizontal translation, (d) large vertical translation.

by taking the time derivative of motor encoder signals. The robot is controlled using Simulink Real-Time, which allows for programming an EtherCAT controller. The impedance controller runs at 2 kHz.

The robot has two operation modes: the collaborative mode and the task mode. In the collaborative mode, a human operator is able to move the end-effector freely to teach a pose or a trajectory. The collaborative mode is obtained by setting $\boldsymbol{K} = \boldsymbol{0}$, $\boldsymbol{D} = \boldsymbol{0}$ and $\boldsymbol{t}_* = \boldsymbol{0}$. Hence, gravity is compensated for, and the operator only feels the inertia of the moving parts and damping. Since the inertia reflected at the platform is very low — due to the low reduction ratio at the actuators and the lightweight moving links — the interaction between the operator and the robot has a very low impedance and a very high bandwidth. In task mode, the stiffness matrix $\boldsymbol{K}$ is positive definite, and the robot replays/repeats the taught poses or trajectories, or simply executes programmed trajectories. The switching between both operation modes is performed using a remote controller.

The damping matrix $\boldsymbol{D}$ is tuned at zero stiffness by increasing the diagonal coefficients. The value is chosen to be as high as possible without yielding a tremorous motion due to the noise on the encoders and the numerical differentiation. The stiffness matrix $\boldsymbol{K}$ is tuned using an empirical method. Experiments revealed that the maximum stiffness value for a given degree of freedom is reached when the other stiffnesses are zero. While theoretically there are no restrictions on the maximum stiffness, in practice, there are limitations due to the mechanical compliance of the links and the actuator torque dynamics that does not match the considered dynamic model at high frequency. Then, the coupling between the coefficients can be explained by the coupling between joint coordinates during task-space control. As a result, once the maximum stiffness values are obtained for each degree of freedom independently, they are divided by six for the simultaneous control of all degrees of freedom. The numerical values of the matrices are

$$\boldsymbol{D} = \begin{bmatrix} 2.25\boldsymbol{I}_3 & \boldsymbol{0} \\ \boldsymbol{0} & 0.075\boldsymbol{I}_3 \end{bmatrix} \quad \text{and} \quad \boldsymbol{K} = \begin{bmatrix} 600\boldsymbol{I}_3 & \boldsymbol{0} \\ \boldsymbol{0} & 3\boldsymbol{I}_2 \end{bmatrix}. \tag{23}$$

V. Results

For the experiments, the term $\boldsymbol{g}$ in (15) is modified to account for the mass of the moving links. This improves gravity compensation; consequently, with the help of static friction, the robot remains stationary when there is no interaction with the operator in collaborative mode.

The accompanying video illustrates the workspace, motion and pHRI capabilities of the robot: `https://youtu.be/SO68ei6WjrQ`.

A. Task Mode

Experiments validate the large workspace of the robot. The platform reaches a 90° tilt angle (Fig. 5a) and a 75° torsion (Fig. 5b). The platform can move out of the robot footprint (Fig. 5c) and has a large vertical range of motion (Fig. 5d).

With the considered prototype, the end-effector can reach accelerations higher than $2g$ in every direction (see Fig. 6) as desired during the design of the leg mechanism. As for the orientation, the rotational acceleration can be larger than $200\,\mathrm{rad\,s^{-2}}$ for both tilting and torsion (see Fig. 7). Actuator saturation is reached only at moments when the acceleration is high. The fact that actuator torques are not saturating continuously indicates that the internal forces are low despite the absence of force/torque sensors. This illustrates the specificity of our approach, which allows for controlling the internal forces without requiring force/torque sensors.

B. Collaborative Mode

In order to display the interaction wrench during the experiments in collaborative mode, the end-effector is equipped with a force/torque sensor. The data acquired by this sensor are only used for analysis and validation purposes, and, in particular, are not used for the control. In other words, the addition of the force/torque sensor has no impact on the behaviour of the robot.

In the video accompanying the paper, the operator imposes sinusoidal-like motions to the end-effector (see Fig. 8). A $2g$ acceleration is reached in every direction during the experiment. The actuator torque remains approximately constant. This torque corresponds to gravity compensation and internal forces due to the mismatch between the considered geometric

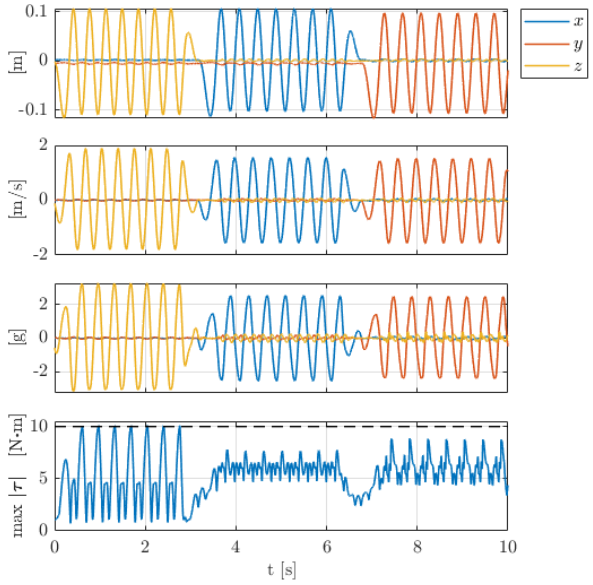

Fig. 6: Cartesian motion of the end-effector. The dashed line is the actuator torque saturation value.

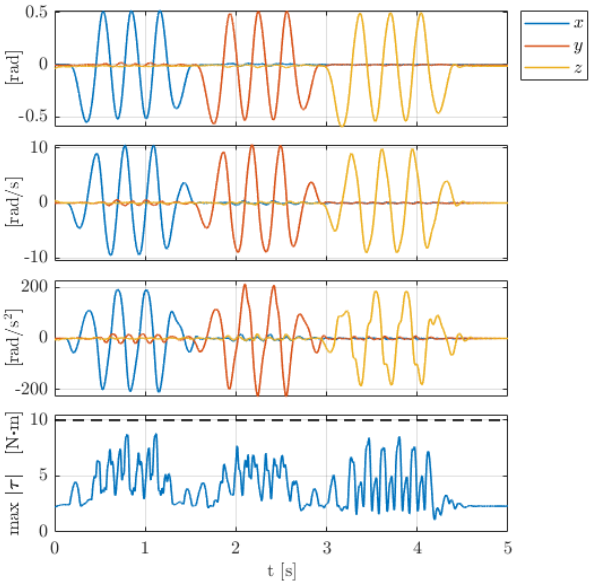

Fig. 7: Angular motion of the end-effector using the angle-axis representation. The dashed line is the actuator torque saturation value.

model and the actual behaviour of the robot. Again, this illustrates that our approach does not require force/torque sensors to limit internal forces.

Using the data acquired from the force/torque sensor, it is possible to analyze the reflected admittance of the end-effector during interaction. Fig. 9 shows velocity, acceleration, and force measurements during both a slow and a fast trajectory imposed by an operator. When the operator moves the end-effector slowly, the interaction force is approximately in phase with the velocity. On the other hand, during faster motion, the interaction force is in phase with the acceleration. This is consistent with the standard admittance model $Y(s) = 1/(ms + d)$, since $Y(0) = 1/d$ and $sY(s) \underset{s\to+\infty}{\sim} 1/m$.

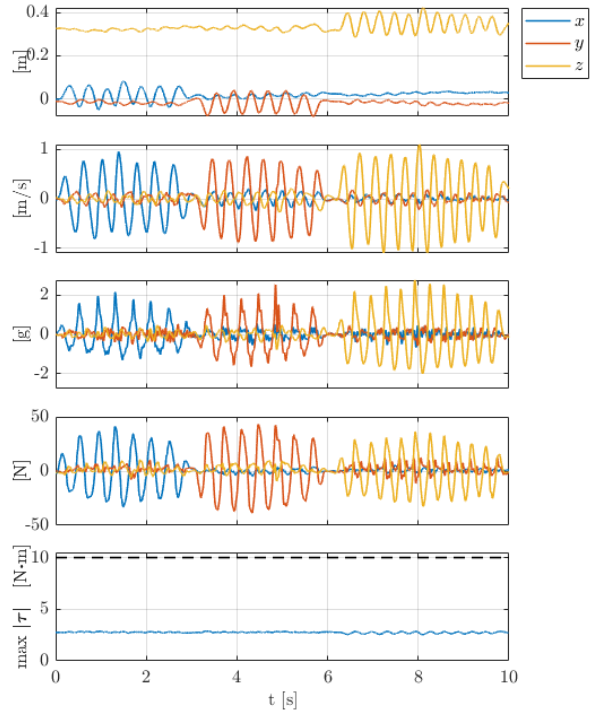

Fig. 8: Cartesian motion in collaborative mode. The dashed line is the actuator torque saturation value.

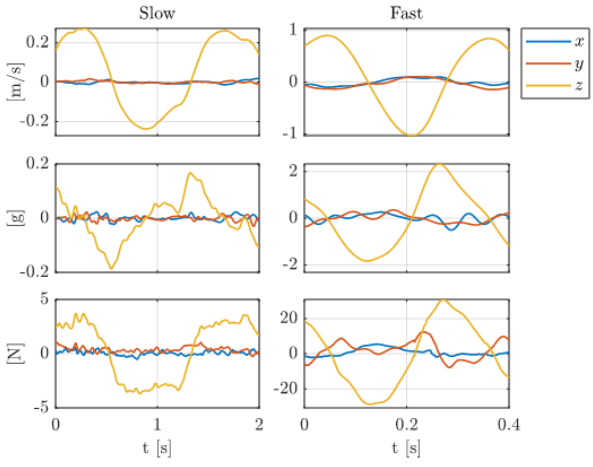

Fig. 9: Slow and fast motion in collaborative mode.

Virtual walls are implemented to demonstrate the possibility of using the robot as a haptic device. If the end-effector reaches positions that are outside of a prescribed

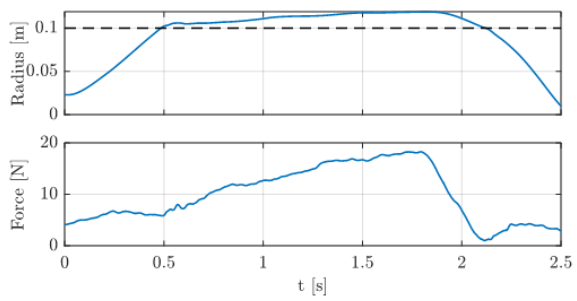

Fig. 10: Virtual wall experiment. The dashed line is the limit.

vertical cylinder, the controller sets the stiffness and damping matrices to the non-zero values used in task mode (23), and selects the reference position $\boldsymbol{p}_*$ by projecting the actual position $\boldsymbol{p}$ onto the surface of the cylinder. The case with a $0.1\,\mathrm{m}$ radius is illustrated in Fig. 10: it can be observed that when the end-effector is outside of the cylinder, the interaction force increases significantly.

VI. Conclusion and Perspectives

In this paper, we propose a novel redundantly actuated parallel robot for sensorless pHRI. Thanks to the redundant design, the robot has few parallel singularities. Therefore, it has a large workspace, especially for orientation. Using backdrivable legs and quasi-direct-drive actuation, the internal antagonistic forces can be controlled without requiring any force/torque sensor. Experiments validate the large workspace of the robot and its pHRI capabilities.

The proposed sensorless control approach offers a clear simplification of the hardware architecture by shifting complexity toward the modelling and control layers; however, this benefit comes at the cost of requiring high-fidelity models. As a perspective, a thorough analysis of the method's robustness with respect to parametric uncertainties and external disturbances is necessary. Such an investigation would provide deeper insight into the practical limits of the approach and help assess its reliability in real-world operating conditions.

Acknowledgement

The authors would like to thank David Breton, Thierry Laliberté and Nicolas Breton for their contributions to the experimental setup.

References

[1] S. Martin and N. Hillier, "Characterisation of the Novint Falcon haptic device for application as a robot manipulator," in *Australasian Conference on Robotics and Automation (ACRA)*, Sydney, Australia, 2009.

[2] P. Lambert and J. L. Herder, "A 7-DOF redundantly actuated parallel haptic device combining 6-DOF manipulation and 1-DOF grasping," *Mechanism and Machine Theory*, vol. 134, pp. 349–364, 2019.

[3] P. Lambert, L. Da Cruz, and C. Bergeles, "Design, Modeling, and Implementation of a 7-DOF Cable-Driven Haptic Device With a Configurable Cable Platform," *IEEE Robotics and Automation Letters*, vol. 5, no. 4, pp. 5764–5771, 2020.

[4] L. Notash and L. Huang, "On the design of fault tolerant parallel manipulators," *Mechanism and Machine Theory*, vol. 38, no. 1, pp. 85–101, 2003.

[5] L.-T. Schreiber and C. Gosselin, "Exploiting the Kinematic Redundancy of a (6 + 3) Degrees-of-Freedom Parallel Mechanism," *ASME Journal of Mechanisms and Robotics*, vol. 11, no. 2, 2019.

[6] J. Lacombe and C. Gosselin, "Singularity analysis of a kinematically redundant (6+2)-DOF parallel mechanism for zero-torsion configurations," *Mechanism and Machine Theory*, vol. 170, p. 104682, 4 2022.

[7] K. Wen, T. S. Nguyen, D. Harton, T. Laliberté, and C. Gosselin, "A Backdrivable Kinematically Redundant (6+3)-Degree-of-Freedom Hybrid Parallel Robot for Intuitive Sensorless Physical Human-Robot Interaction," *IEEE Transactions on Robotics*, vol. 37, no. 4, pp. 1222–1238, 2021.

[8] A. Yiğit, D. Breton, and C. Gosselin, "Exploiting the Kinematic Redundancy of a (6 + 3)-Degree-of-Freedom Parallel Manipulator to Produce Unlimited Rotation of the Platform," *Journal of Mechanisms and Robotics*, vol. 16, no. 7, 7 2024.

[9] A. Yiğit, T.-S. Nguyen, and C. Gosselin, "Exploiting the Kinematic Redundancy of a Backdrivable Parallel Manipulator for Sensing During Physical Human-Robot Interaction," in *2023 IEEE/RSJ International Conference on Intelligent Robots and Systems (IROS)*. IEEE, 10 2023, pp. 9788–9793.

[10] A. Mueller, "Redundant Actuation of Parallel Manipulators," in *Parallel Manipulators, towards New Applications*. I-Tech Education and Publishing, 4 2008.

[11] C. Gosselin and L.-T. Schreiber, "Redundancy in Parallel Mechanisms: A Review," *Applied Mechanics Reviews*, vol. 70, no. 1, 2018.

[12] Hui Cheng, Yiu-Kuen Yiu, and Zexiang Li, "Dynamics and control of redundantly actuated parallel manipulators," *IEEE/ASME Transactions on Mechatronics*, vol. 8, no. 4, pp. 483–491, 2003.

[13] F. Firmani and R. P. Podhorodeski, "Force-unconstrained poses for a redundantly-actuated planar parallel manipulator," *Mechanism and Machine Theory*, vol. 39, no. 5, pp. 459–476, 2004.

[14] R. Kurtz and V. Hayward, "Multiple-goal kinematic optimization of a parallel spherical mechanism with actuator redundancy," *IEEE Transactions on Robotics and Automation*, vol. 8, no. 5, pp. 644–651, 1992.

[15] S. Kim, "Operational quality analysis of parallel manipulators with actuation redundancy," in *Proceedings of the IEEE International Conference on Robotics and Automation*, vol. 3, 1997, pp. 2651–2656.

[16] A. Mueller, "Internal Preload Control of Redundantly Actuated Parallel Manipulators—Its Application to Backlash Avoiding Control," *IEEE Transactions on Robotics*, vol. 21, no. 4, pp. 668–677, 8 2005.

[17] T. Harada and P. Liu, "Internal and External Forces Measurement of Planar 3-DOF Redundantly Actuated Parallel Mechanism by Axial Force Sensors," *ISRN Robotics*, vol. 2013, pp. 1–8, 2013.

[18] T. Harada and M. Nagase, "Impedance control of a redundantly actuated 3-DOF planar parallel link mechanism using direct drive linear motors," in *Proceedings of the IEEE International Conference on Robotics and Biomimetics*, 2010, pp. 501–506.

[19] A. Yigit, D. Breton, Z. Zhou, T. Laliberté, and C. Gosselin, "Kinematic Analysis and Design of a Novel (6+3)-DoF Parallel Robot with Fixed Actuators," in *Proceedings of the IEEE International Conference on Robotic and Automation*, 5 2023, pp. 9693–9699.

[20] A. Yiğit, S. Foucault, T. Laliberté, D. Breton, Z. Zhou, and C. Gosselin, "Parallel robot with proprioceptive actuation for low-impedance sensorless pHRI," *Control Engineering Practice*, vol. 169, 4 2026.

[21] K. Wen and C. Gosselin, "Kinematically Redundant Hybrid Robots With Simple Singularity Conditions and Analytical Inverse Kinematic Solutions," *IEEE Robotics and Automation Letters*, vol. 4, no. 4, pp. 3828–3835, 2019.

[22] Z. Zhou and C. Gosselin, "Analysis and Design of a Novel Compact Three-Degree-of-Freedom Parallel Robot," *ASME Journal of Mechanisms and Robotics*, vol. 15, no. 5, 10 2023.

[23] C. Gosselin and J. Angeles, "Singularity analysis of closed-loop kinematic chains," *IEEE Transactions on Robotics and Automation*, vol. 6, no. 3, pp. 281–290, 1990.

[24] F. Caccavale, C. Natale, B. Siciliano, and L. Villani, "Six-DOF impedance control based on angle/axis representations," *IEEE Transactions on Robotics and Automation*, vol. 15, no. 2, pp. 289–300, 4 1999.

[25] L.-T. Schreiber and C. Gosselin, "Passively Driven Redundant Spherical Joint With Very Large Range of Motion," *ASME Journal of Mechanisms and Robotics*, vol. 9, no. 3, 2017.